Resonance in the K2-19 system is at odds with its high reported eccentricities

Antoine C Petit, Erik A Petigura, Melvyn B Davies, Anders Johansen

Monthly Notices
of the
ROYAL ASTRONOMICAL SOCIETY

MNRAS **496,** 3101–3111 (2020)
Advance Access publication 2020 June 18

doi:10.1093/mnras/staa1736

Resonance in the K2-19 system is at odds with its high reported eccentricities

Antoine C. Petit [1,2★] Erik A. Petigura [3] Melvyn B. Davies[1] and Anders Johansen[1]

[1]*Lund Observatory, Department of Astronomy and Theoretical Physics, Lund University, P.O. Box 43, SE-22100 Lund, Sweden*
[2]*IMCCE, CNRS-UMR8028, Observatoire de Paris, PSL University, Sorbonne Université, 77 Avenue Denfert-Rochereau, F-75014 Paris, France*
[3]*Department of Physics and Astronomy, University of California Los Angeles, Los Angeles, CA 90095, USA*

Accepted 2020 June 11. Received 2020 June 11; in original form 2020 March 10

ABSTRACT

K2-19 hosts a planetary system composed of two outer planets, b and c, with size of 7.0 ± 0.2 $R_\oplus$ and 4.1 ± 0.2 $R_\oplus$, and an inner planet, d, with a radius of $1.11 \pm 0.05\,R_\oplus$. A recent analysis of Transit-Timing Variations (TTVs) suggested b and c are close to but not in 3:2 mean motion resonance (MMR) because the classical resonant angles circulate. Such an architecture challenges our understanding of planet formation. Indeed, planet migration through the protoplanetary disc should lead to a capture into the MMR. Here, we show that the planets are in fact, locked into the 3:2 resonance despite circulation of the conventional resonant angles and aligned periapses. However, we show that such an orbital configuration cannot be maintained for more than a few hundred million years due to the tidal dissipation experienced by planet d. The tidal dissipation remains efficient because of a secular forcing of the innermost planet eccentricity by planets b and c. While the observations strongly rule out an orbital solution where the three planets are on close to circular orbits, it remains possible that a fourth planet is affecting the TTVs such that the four planet system is consistent with the tidal constraints.

Key words: celestial mechanics – planets and satellites: dynamical evolution and stability – planets and satellites: formation – planets and satellites: individual: (K2-19b, K2-19c, K2-19d).

1 INTRODUCTION

The numerous planet discoveries over the past decades have revealed the large diversity in sizes and orbital architecture of exoplanetary systems (Winn & Fabrycky 2015). The discovery of Hot Jupiters (Mayor & Queloz 1995) and of super-Earths have profoundly changed how we see planets and their formation outside of the Solar system narrative. Since then, planet formation theories have been adapted to take this diversity into account. The models now prefer a fast formation within the protoplanetary disc lifetime involving a migration process (e.g. Bitsch et al. 2019; Izidoro et al. 2019; Lambrechts et al. 2019, and references therein). In particular, the migration process can lead to the capture of planet in mean motion resonant (MMR) chains (Cresswell & Nelson 2008). Most of the resonant chains are expected to break once the protoplanetary disc is dissipated as most of the systems are observed outside of MMR (Izidoro et al. 2017, 2019). Nevertheless, the period ratio distribution still shows signpost of this past history (Fabrycky et al. 2014). The study of the few remaining resonant chains is thus of particular interest to unravel the very early life of planetary systems.

The capture into MMR is a complex process that depends on the migration parameters, the planet masses and the particular resonance where capture happen (e.g. Mustill & Wyatt 2011; Batygin 2015). Nevertheless, we expect planets in resonant chains to have close to circular orbits due to the eccentricity damping during the migration (Cresswell & Nelson 2008). Such configurations have been observed for various systems observed through both radial velocities (RV) and with the analysis of Transit-Timing Variations (TTV, see e.g. Agol et al. 2005; Holman & Murray 2005). Systems where observations challenge this theoretical picture are of particular interest as they are the only way to probe the validity and/or the generality of theories.

K2-19 hosts three known transiting planets. The first two were reported (Armstrong et al. 2015) based on the photometry collected by the *Kepler Space Telescope* during the *K2* operations (Howell et al. 2014). K2-19 b and c appeared to be close to the 3:2 MMR, but it was not possible to conclude whether or not the pair was indeed in resonance. Planets b and c sizes lies between Uranus and Saturn with respective radii of 7.0 ± 0.2 and 4.1 ± 0.2 $R_\oplus$ and they orbit in respectively 7.9 and 11.9 d. A third inner planet was

★ E-mail: antoine.petit@astro.lu.se

detected by Sinukoff et al. (2016). Planet d orbits in 2.5 d and has a size similar to Earth with a radius of $1.11 \pm 0.05\,R_\oplus$. The recent observations by Petigura et al. (2020) of TTV for both planets b and c, as well as RV measurements showing the reflex motion due to planet b, have given a precise set of orbital elements for the system. The 5 per cent fractional uncertainties, are among the smallest for sub-Jovian exoplanets. Using a photodynamical model, they obtained a determination of the planet masses and orbital element down to a few per cent. One puzzling aspect of this system is the moderate eccentricities of 0.2 with well-aligned apsides ($\Delta\varpi = 2 \pm 2^\circ$) of planets b and c. Petigura et al. (2020) conclude from these observations that the system is very close to the 3:2 commensurability while not being resonant based on the analysis of the classical resonant angles. K2-19 system's architecture is thus puzzling from a dynamical point of view as no clear mechanism is identified to explain its stability. Indeed, Petigura et al. (2020) report that the system is stable in numerical simulations but is strongly angular momentum deficit (AMD) unstable (Laskar & Petit 2017) and not protected by the resonance. Moreover, such a configuration is in tension with our current understanding of planet formation. Indeed, convergent migration within the protoplanetary disc leads to eccentricity damping and capture into MMR (Cresswell & Nelson 2008). The planets trapped into such state have low eccentricity (comparable to the protoplanetary disc aspect ratio $\simeq$0.05) and have their periapses anti-aligned (Batygin & Morbidelli 2013).

The dynamics of the system and its origin thus necessitate an in-depth study. From a dynamical point of view, the proximity to the resonance and the eccentric and aligned orbits require one to go beyond the simple study of the resonant angles as they may not be representative of the nature of the dynamics. Given that all the planets are within 0.1 au, tidal effects must also be considered.

In this paper, we revisit the dynamical study of the system orbiting K2-19. We show in Section 2 that the two outer planets are indeed trapped into the 3:2 MMR despite being apsidally aligned and the resonant angles circulation. The first-order resonant model explains all the dynamics properties discussed by Petigura et al. (2020). We also show that the inner planet is secularly coupled to the b–c pair. We then study in Section 3 the effect of tidal dissipation on to the inner planet d. We show that due to the eccentricity forcing from the outer planets, planet d's orbit tends to decay while the outer planets circularize. The time-scale for the system evolution is shorter than its lifetime rendering the configuration unlikely. In these two sections, we take the results from Petigura et al. (2020) as certain and simply draw conclusions based on the dynamical analysis. We finally discuss in Section 4 the tension between the observations and our theoretical understanding of the system history. In particular, we highlight the constraints on the three planet best fit and discuss whether the TTVs might be affected by an unmodelled effect, including the presence of a planet not yet detected.

2 RESONANT DYNAMICS OF K2-19'S SYSTEM

In this section, we re-analyse the dynamics of the best-fitting three planet solution given by Petigura et al. (2020). We show that the outer planets are indeed inside the MMR and that they are coupled secularly to the inner planet. We partially reproduce in Table 1, the orbital elements and planet characteristics from the best photodynamical fit from Petigura et al. (2020).

Table 1. K2-19 system parameters from Petigura et al. (2020), reproduced by permission of the AAS.

Parameter	Value
$M_\star$ ($M_\odot$)	0.88 ± 0.03
$R_\star$ ($R_\odot$)	0.82 ± 0.03
P_b (d)	7.9222 ± 0.0001
$T_{c,b}$ (BJD−2454833)	2027.9023 ± 0.0002
$\sqrt{e_b}\cos\omega_b$	0.02 ± 0.06
$\sqrt{e_b}\sin\omega_b$	-0.44 ± 0.04
i_b (deg)	91.5 ± 0.1
Ω_b (deg)	0 (fixed)
$R_{p,b}/R_\star$	0.0777 ± 0.0006
$M_{p,b}$ ($M_\oplus$)	32.4 ± 1.7
P_c (d)	11.8993 ± 0.0008
$T_{c,c}$ (BJD−2454833)	2020.0007 ± 0.0004
$\sqrt{e_c}\cos\omega_c$	0.04 ± 0.04
$\sqrt{e_c}\sin\omega_c$	-0.46 ± 0.03
i_c (deg)	91.1 ± 0.1
Ω_c (deg)	-7.4 ± 0.8
$R_{p,c}/R_\star$	0.0458 ± 0.0004
$M_{p,c}$ ($M_\oplus$)	10.8 ± 0.6
P_d (d)	2.5081 ± 0.0002
$T_{c,d}$ (BJD−2454833)	2021.0726 ± 0.0018
$\sqrt{e_d}\cos\omega_d$	0 (fixed)
$\sqrt{e_d}\sin\omega_d$	0 (fixed)
i_d (deg)	90.8 ± 0.7
Ω_d (deg)	0 (fixed)
$R_{p,d}/R_\star$	0.0124 ± 0.0004
$M_{p,d}$ ($M_\oplus$)	<10
Derived parameters	
$R_{p,b}$ ($R_\oplus$)	7.0 ± 0.2
$R_{p,c}$ ($R_\oplus$)	4.1 ± 0.2
$R_{p,d}$ ($R_\oplus$)	1.11 ± 0.05
e_b	0.20 ± 0.03
e_c	0.21 ± 0.03
$\Delta\omega$ (deg)	2 ± 2

2.1 The 3:2 mean motion resonance

The analysis of the K2 photometric data makes it clear that K2-19 b and c are close to the 3:2 MMR. Being close to the 3:2 MMR means that the planet mean motions $n_k = 2\pi/P_k$ (P_k being the planets' orbital periods) satisfy the arithmetic relation $2n_b - 3n_c \simeq 0$. As a result, the motion of the planets are coupled and one cannot average over the fast motions to study the long-term orbital evolution. Instead, the classical approach to analyse resonant motions consists of averaging the planet interactions over the non-resonant angles to reduce the problem to a one degree of freedom problem that is integrable. For first-order MMR such as the 3:2 resonance, d'Alembert relations (see Morbidelli 2002) impose that at first order, the resonant terms in the development of the perturbation depend on the angles

$$\varphi_k = 2\lambda_b - 3\lambda_c + \varpi_k \tag{1}$$

where λ_k and ϖ_k are respectively the mean longitude and the longitude of the periapsis of planet k. There are two different combination of angles related to the 3:2 resonance. In principle, the interaction between the two terms should make the system not integrable. In reality, the system can be reduced to a one degree of freedom resonant system thanks to a constant of motion that appears after a canonical transformation (Sessin & Ferraz-Mello 1984; Henrard et al. 1986).

The integrable approximation for first-order MMR has been called the second fundamental model of resonance[1] (Henrard & Lemaitre 1983). The analytical derivation of the integrable model for two massive planets has been carried out by several authors (Henrard et al. 1986; Batygin & Morbidelli 2013; Deck, Payne & Holman 2013; Delisle, Laskar & Correia 2014; Petit, Laskar & Boué 2017; Hadden 2019). It is obtained by an expansion to first order in eccentricity, averaging over the fast angle and a rotation of the two classical resonant coordinates

$$x_k = \sqrt{C_k} e^{\imath(\varpi_k - \theta_{\rm res})} \simeq \sqrt{\frac{\Lambda_k}{2}} e_k e^{\imath(\varpi_k - \theta_{\rm res})} \tag{2}$$

where $C_k = \Lambda_k(1 - \sqrt{1-e_k^2})$ is the AMD (Laskar 1997) of the planet k, $\Lambda_k = m_k\sqrt{\mathcal{G}m_S a_k}$, $\mathcal{G}$ is the gravitational constant, and $\theta_{\rm res} = 3\lambda_c - 2\lambda_b$. Following Petit et al. (2017), we also define

$$\tilde{e}_k = \sqrt{\frac{2C_k}{\Lambda_k}} = \sqrt{2\left(1 - \sqrt{1-e_k^2}\right)} \simeq e_k. \tag{3}$$

The rotation, first described in Sessin & Ferraz-Mello (1984), transforms the coordinates x_b, x_c into two complex coordinates y_1 and y_2 (we follow here the notations from Petit et al. 2017). The norm of y_2 is a constant of motion and the dynamics of y_1 are described by the second fundamental model of resonance (see Ferraz-Mello 2007, for a complete description of the dynamics). It is also worth pointing out that the total AMD of the system is given by $C = I_1 + I_2$ where $I_k = y_k\bar{y}_k$. For the 3:2 MMR, the expressions of y_1 and y_2 are

$$y_1 = \sqrt{\frac{\Lambda_b}{2}} \frac{\tilde{e}_b e^{\imath\varpi_b} - 1.22\tilde{e}_c e^{\imath\varpi_c}}{\sqrt{1+1.31\gamma}} e^{-\imath\theta_{\rm res}}, \tag{4}$$

$$y_2 = \sqrt{\frac{\Lambda_c}{2}} \frac{1.07\gamma\tilde{e}_b e^{\imath\varpi_b} + \tilde{e}_c e^{\imath\varpi_c}}{\sqrt{1+1.31\gamma}} e^{-\imath\theta_{\rm res}}, \tag{5}$$

where $\gamma = m_b/m_c \simeq 3.0$ for K2-19 and the numerical coefficients come from the expansion of the resonant terms of the 3:2 resonance. More precisely, the coefficients are linear combinations of different Laplace coefficients evaluated at the exact Keplerian resonance. We give the analytical expression in Appendix A and refer to Batygin & Morbidelli (2013), Petit et al. (2017) or Hadden (2019) for recent complete derivations of the Hamiltonian.

Without loss of generality, one may rescale y_1 and y_2

$$Y_1 = \sqrt{\frac{2}{\Lambda_b}} y_1 = \frac{\tilde{e}_b e^{\imath\varpi_b} - 1.22\tilde{e}_c e^{\imath\varpi_c}}{\sqrt{1+1.31\gamma}} e^{-\imath\theta_{\rm res}}, \tag{6}$$

$$Y_2 = \sqrt{\frac{2}{\Lambda_c}} y_2 = \frac{1.07\gamma\tilde{e}_b e^{\imath\varpi_b} + \tilde{e}_c e^{\imath\varpi_c}}{\sqrt{1+1.31\gamma}} e^{-\imath\theta_{\rm res}}. \tag{7}$$

They are linear combinations of the eccentricities where Y_1 is roughly the eccentricity vectors difference and Y_2 the mass weighted sum. The posterior distributions for Y_1 and Y_2 calculated from Petigura et al. (2020) are shown in Fig. 1. As we can see, Y_1 is much more constrained than Y_2.

In the case of a system with two massive planets, the real resonant angle corresponds to the argument of Y_1. Hence, to determine if the system is indeed in resonance one should in principle verify if the variable Y_1 evolves within the resonant island shown in Fig. 2. In reality, for most of the resonant chains observed in exoplanet systems, the resonant angles φ_k (equation 1) are good proxies for the actual resonant angle and such an analysis is not needed (see below).

[1]The first fundamental model is the classical pendulum.

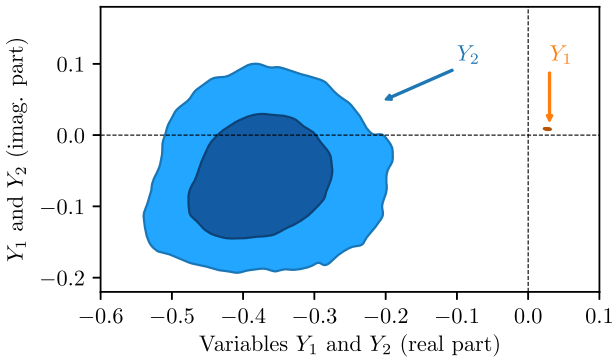

Figure 1. Posterior distribution of the real and imaginary parts of Y_1 and Y_2 calculated from Petigura et al. (2020). Colours correspond to the 1σ and 2σ confidence levels. The posterior distribution of Y_1 is plotted to show the differences in uncertainties.

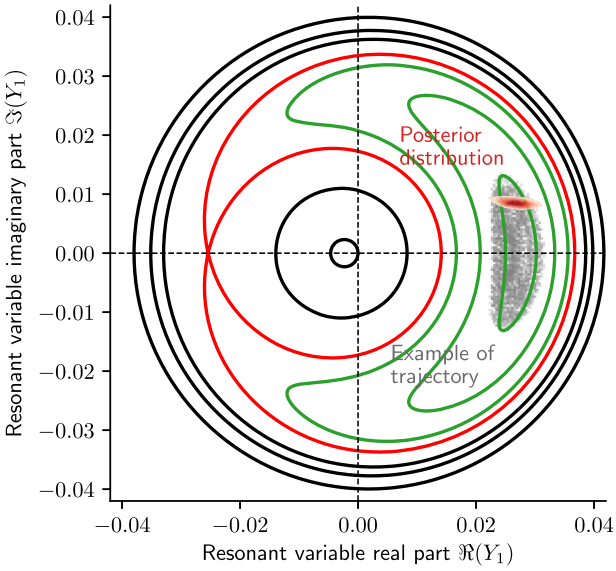

Figure 2. Phase portrait of the integrable approximate Hamiltonian in the Y_1 (equation 6) space. The black lines correspond to circulating orbits, the green lines to resonant orbits, and the red line is the separatrix. The red set represents the posterior probability distribution of Y_1 at time $t = 2020$ BJD − 2454833. The grey points corresponds to the result of one N-body integration of the two-planet system for 5000 planet b orbits.

On the other hand, the actual value of Y_2 is less critical to determine whether or not the system is resonant because it does not affect directly the shape of the resonance (Fig. 2). It can also be shown (see Appendix A) that within the limit of the first order model, Y_2 precesses at the same frequency as $\theta_{\rm res}$. Hence, $Y_2 e^{\imath\theta_{\rm res}}$ is almost a constant that we will note

$$\tilde{Y}_2 = Y_2 e^{\imath\theta_{\rm res}} = \frac{1.07\gamma\tilde{e}_b e^{\imath\varpi_b} + \tilde{e}_c e^{\imath\varpi_c}}{\sqrt{1+1.31\gamma}}. \tag{8}$$

In reality, secular terms are neglected in this approximation. Nevertheless, the evolution of $\tilde{Y}_2$ happens on a much longer time-scale.

The phase space dynamics of Y_1 are shown in Fig. 2. We compute the phase portrait using the expression of the Hamiltonian given in the appendix (equation A16). We also plot the distribution of Y_1 using the posterior distribution of Petigura et al. (2020). It should

be noted that while the uncertainties on the eccentricities are of the order of 0.03 in this paper, Y_1 has a much more restricted spread, reinforcing the argument that the system is in a resonant state, that is the data require that Y_1 is well-within the resonant island shown in Fig. 2. Finally, we plot the result of a numerical integration of the two-planet system. We integrated multiple draws from the posterior distribution from Petigura et al. (2020) with `REBOUND` (Rein & Liu 2012) and the high order integrator `SABA(10,6,4)` (Blanes et al. 2013; Rein, Tamayo & Brown 2019) and for 5000 orbits of planet b (roughly 108 yr). We show a sample trajectory in Fig. 2. All draws behaved in qualitatively the same way, that is showing the libration of the resonant variable Y_1.

It is clear that the dynamics are resonant, moreover, we can see that all the trajectories lie very close to the centre of the resonance. It suggests that the mechanism that led to the capture must have been gentle and dissipative (Batygin 2015). The most favoured mechanism for the formation is through migration within a protoplanetary disc (e.g. Cresswell & Nelson 2008). However, such a scenario is incompatible with the large eccentricities as well as the apsidal alignment of planet b and c as discussed in Petigura et al. (2020).

2.2 Short-term eccentricity evolution

Petigura et al. (2020) also reported that e_b and e_c oscillate over a period of about 6 yr. We show that this oscillation is well explained by the resonant dynamics.

In most of the systems that have been observed in resonant configurations, Y_2 is usually negligible with respect to Y_1. When $|Y_2| \ll |Y_1|$, the libration of the angles φ_k (equation 1) is a good proxy to test whether or not a system is in MMR. However, in cases where Y_2 cannot be neglected with respect to Y_1, the transformation from this set of resonant variables to the classical orbital elements is not straightforward. This means that the angles φ_k can circulate while the system is actually very well described by the resonant first-order integrable model. Indeed, the inverse transformation from Y_k to the complex eccentricities can be written as

$$\tilde{e}_b e^{\imath(\varpi_b - \theta_{\rm res})} = \frac{Y_1 + 1.22 Y_2}{\sqrt{1 + 1.31\gamma}},$$
$$\tilde{e}_c e^{\imath(\varpi_c - \theta_{\rm res})} = \frac{-1.07\gamma Y_1 + Y_2}{\sqrt{1 + 1.31\gamma}}. \quad (9)$$

Since Y_1 oscillates around the resonant centre, its argument is librating. In a very rough approximation, we can consider it as constant. On the other hand, Y_2 has a constant norm and is rotating, with a frequency comparable to the one of $\theta_{\rm res}$ that can be approximated as

$$\nu_\theta = -3\delta n_c \simeq -2.7 \times 10^{-3}\ \mathrm{rad\,d^{-1}}, \quad (10)$$

where $\delta = 2n_b/(3n_c) - 1$, represents the distance to the exact Keplerian resonance. In this approximation, $\tilde{e}_b e^{\imath(\varpi_b - \theta_{\rm res})}$ describes a circle centred on $Y_1/\sqrt{1+1.31\gamma}$ and of radius $1.22Y_2/\sqrt{1+1.31\gamma}$ (a similar analysis can be done for planet c). The angle $\varphi_b = \varpi_b - \theta_{\rm res}$ librates if the complex plane origin lies outside of this circle. From equation (9), we see that if $|Y_1| \lesssim 1.22|Y_2|$ (respectively, $1.07\gamma|Y_1| \lesssim |Y_2|$), then $\varphi_b = \varpi_b - \theta_{\rm res}$ (respectively, $\varphi_c = \varpi_c - \theta_{\rm res}$) circulates. In the case of the best fit studied here, both of these conditions are fulfilled. As a result, we cannot use the classical angles to probe the resonance. To our knowledge, this is the first system observed where the resonance cannot be characterized thanks to the classical angles.

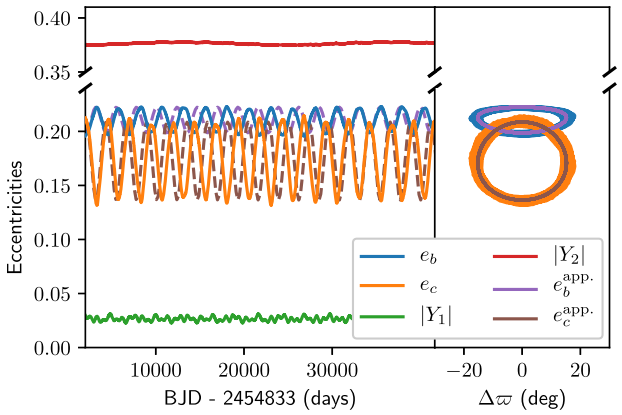

Figure 3. Dynamical evolution of the eccentricities and resonant variables of the numerical solution described in Section 2.1. The quantities Y_k are defined by equations (6) and (7) and $e_k^{\rm app.}$ by equation (11).

The 3:2 resonance can also explain the eccentricity dynamics and in particular the apsidal aligned configuration. Let us denote with Y_1^0 and Y_2^0 the initial conditions for Y_1 and Y_2 at t_0, the evolution of the eccentricities can be approximated as

$$e_b e^{\imath\varpi_b} \simeq 0.46 Y_1^0 e^{-\imath\nu_\theta(t-t_0)} + 0.56 Y_2^0,$$
$$e_c e^{\imath\varpi_c} \simeq -1.40 Y_1^0 e^{-\imath\nu_\theta(t-t_0)} + 0.46 Y_2^0, \quad (11)$$

where γ was replaced by its average value and we used the approximation $\tilde{e}_k \simeq e_k$. From equation (11), we see that the oscillations of e_c are about three times as large as the one of e_b. The period of oscillations should be of order 6.3 yr.

We plot in Fig. 3 the evolution of the eccentricities of planet b and c, of $|Y_1|$ and $|Y_2|$ as well as the approximation from equation (11). While there is a small discrepancy on the frequency (the error is of the order of 10 per cent), the amplitude of the motion is well reproduced. Moreover, the agreement in the plane e_k–$\Delta\varpi$ is very good.

The main observational evidence for the resonance comes from the TTV. While the eccentricities evolve with a period of about 6 yr, the main frequency in the observed TTVs from Petigura et al. (2020) is about 2 yr, which is the period of the oscillation of the resonant variable Y_1.

2.3 Secular evolution

On short time-scales (i.e. comparable to the TTV baseline), the simple model described above gives a good description of the system dynamics. On longer time-scales (more than a few kyr), the system is subject to orbital precession due to secular interactions. We integrate the same initial condition as in the previous section, but this time we add planet d to the system. The initial condition was drawn from the posterior distribution and the mass of planet d in this particular realization[2] is 5.9 $M_\oplus$. The simulation is run for 10 000 yr, general relativity and stellar oblateness slightly change the precession rate but are not included in the example shown.

We plot the eccentricities as well as $|Y_1|$ and $|Y_2|$ in Fig. 4. We see that as in the case with only planets b and c, the eccentricities e_b and e_c evolve very rapidly with the roughly 6 yr period seen

[2]The value is close to the average of the posterior distribution but results were qualitatively similar for other realizations (not shown here).

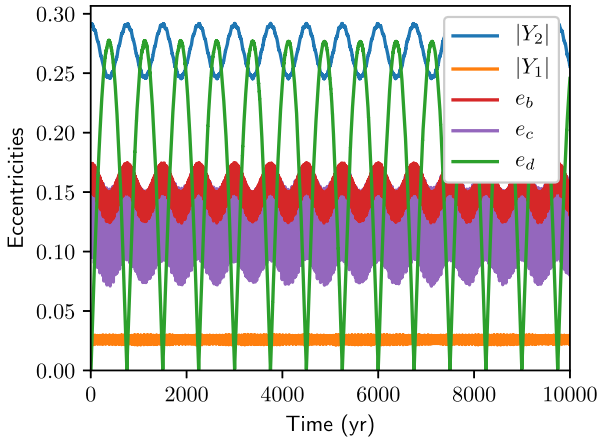

Figure 4. Eccentricities dynamical evolution over long time-scales when planet d is included.

in Section 2.2, while $|Y_1|$ is almost constant. We checked that the resonance is indeed preserved in this case during the whole integration. However, $|Y_2|$ is no longer a constant and there are large AMD exchanges between planet d and the b–c pair. Due to the smaller planet d mass and semimajor axis, its eccentricity rises to values around 0.37 and its mean value is 0.24. We conclude that even starting with a circular orbit, planet d is largely coupled to the two outer planets and therefore cannot be considered in isolation.

3 TIDAL DECAY DURING LONG-TERM EVOLUTION

From the last section, we have seen that K2-19's system is stable over long time-scales. But until now we have only taken into account the purely *N*-body gravitational interactions. However, due to their eccentric orbits, the three planets are subject to tidal effects. Indeed, the change of orbital distance leads to friction inside the planet and thus energy dissipation. Tidal effects conserve the total angular momentum[3] (Goldreich & Soter 1966). The energy loss results in a circularization of the orbits and a decay of the semimajor axes.

Dissipative effects are of particular importance due to the estimated age of the system. Indeed, based on K2-19's rotation period, the star is older than 1 Gyr. Besides, an age of a few Gyr is compatible with the rotation rate and effective temperature (Trevor, private communication: the star is more slowly rotating so more likely older than similar temperature 1 Gyr old stars).

3.1 Low-eccentricity tidal migration

Pu & Lai (2019) proposed a formation mechanism for ultrashort-period planets (with an orbital period of around 1 d), that they called the low-eccentricity migration scenario (see also Mardling 2007; Laskar, Boué & Correia 2012). They showed that, in a multiplanetary system with slightly eccentric outer planets, the inner planet migrates very efficiently inward up until the point where it is decoupled due to the precession induced by the star oblateness and general relativity or if the outer planets run out of AMD.

[3]In this analysis, we neglect the planets spin as well as tides raised on the star, that influences the stellar spin. The total *orbital* angular momentum is thus conserved

Since planet b and c interact secularly with planet d only through the variation of Y_2, we will assume that the interaction can be reduced to a two planet case: planet d and an outer planet. This simplification does not affect the results since the resonance is not affected by a variation of Y_2 (see Fig. 4). We use the two planet model presented by Pu & Lai (2019) to compute the effect of tides on planet d's orbit. It should be noted that considering the two outer planet as a single one is a conservative assumption as their interactions could lead to a faster migration (Pu & Lai 2019).

Following the weak friction theory of equilibrium tides (Darwin 1880; Alexander 1973; Hut 1981; Pu & Lai 2019), the evolution of the planets' semimajor axes in presence of tides is given by the equation

$$\frac{\dot{a}_k}{a_k} = -1.9\times10^{-9} k_{2,k} \left(\frac{\Delta t_{L,k}}{100\ \mathrm{s}}\right) \left(\frac{e_k}{0.02}\right)^2 \left(\frac{m_S}{M_\odot}\right)^2 \times \left(\frac{m_k}{M_\oplus}\right)^{-1} \left(\frac{R_k}{R_\oplus}\right)^5 \left(\frac{a_k}{0.02\ \mathrm{au}}\right)^{-8} \mathrm{yr}^{-1}, \quad (12)$$

where $k_{2,k}$ is the tidal Love number, $\Delta t_{L,k}$ is the tidal lag time, and R_k is the radius for planet k. We note that the decay time-scale depends on the eccentricity squared. The decay is fast at moderate eccentricity and slows down as the orbit becomes more and more circular. While the eccentricities of the outer planets are not extremely high, the validity of the limitation to leading order in eccentricities in equation (12) should be discussed. From Hut (1981), we remark the the additional terms at order e^4 and e^6 accelerate the dissipation. Besides, while relevant at the beginning (when $e_b \simeq 0.2$) the corrections become negligible for eccentricities closer to 0.1. It results that the equation (12) gives a conservative decay rate and we do not include higher order corrections given the other uncertainties on the system such as on the tidal lag times.

The tides become less important for the farthest planets because of the steep a_k^{-8} dependency. In principle tidal dissipation in the two outer planets should be considered. However, the tidal dissipation in large planets is not well constrained (Ogilvie 2014). We thus follow the conservative assumption made in Pu & Lai (2019) to neglect tides affecting planets b and c.

The decay rate also depends on the two coefficients $k_{2,d}$, of order unity, and $\Delta t_{L,d}$. Using this parametrized formalism allows us to study the dissipation while remaining agnostic on the actual physical mechanisms at play. We show below that the results are compatible with a large range of values for the coefficients. As Pu & Lai (2019), we take $k_{2,d} = 1$. The tidal lag $\Delta t_{L,d}$ is inversely proportional to the planet's quality factor

$$Q_d = \frac{P_d}{4\pi\Delta t_{L,d}}. \quad (13)$$

Planet d is terrestrial so its tidal lag is close to 100 s (Goldreich & Soter 1966; Pu & Lai 2019), which corresponds to a quality factor close to 170. Using values close to the Solar system terrestrial planets is common in the field and motivated by studies of the viscoelastic response of planets to tidal deformations (Correia et al. 2014; Efroimsky & Makarov 2014; Makarov & Efroimsky 2014). In our analysis, we choose to draw planet d tidal lag time from a log-uniform distribution with boundaries $50\ \mathrm{s} \leq \Delta t_{L,d} \leq 500\ \mathrm{s}$.

We first detail our model for the long-term evolution of the system and then discuss the possible outcomes. As shown in Section 2.3, the eccentricity of planet d is driven by its secular coupling with the outer planets. For planet d, we replace in equation (12), the eccentricity e_d by a forced eccentricity $e_{d,\,\mathrm{forced}}$ given by the secular coupling. The forced eccentricity can be estimated as a function of

planets b and c eccentricities. We use equation (40) from Pu & Lai (2019),

$$e_{d,\mathrm{forced}} = \frac{\nu_{d,b}}{\omega_{b,d} + \omega_{d,\mathrm{gr}} + \omega_{d,\mathrm{tide}}} e_b, \tag{14}$$

where $\nu_{d,b}$ and $\omega_{b,d}$ correspond to secular interaction terms between b and d, and $\omega_{d,\mathrm{gr}}$ and $\omega_{d,\mathrm{tide}}$ are respectively the apsidal precession of planet d due to general relativity and tides. While planet d is close to its current position, $a_d \simeq 0.035$ au, the ratio $e_{d,\mathrm{forced}}/e_b$ is close to 0.5. For shorter orbits ($a_d \lesssim 0.01$ au), the ratio sharply decays as general relativity and tidal precession become significant and decouple planet d from the outer planets, effectively stopping the tidal migration. The secular planet interactions are computed using Lagrange–Laplace theory. We do not include higher order terms despite the moderate eccentricities. Indeed, as we see in Fig. 4, planet d eccentricity is well coupled to the pair b–c in numerical simulations. Higher order corrections will most likely give a more accurate coupling, but equation (14) reproduces qualitatively the observed behaviour for moderate eccentricities and is accurate once the eccentricities become smaller.

Finally, the outer planets eccentricities evolve as planet d migrates because tides raised on planets conserve the total orbital angular momentum.[4] One can estimate e_b as a function of the new semimajor axis of planet d, and the initial values for e_b, a_d, and a_b

$$e_b^2 = 1 - \left(1 - \frac{C_0 - (\Lambda_{d,0} - \Lambda_d)}{\Lambda_d + \Lambda_b + \Lambda_c}\right)^2, \tag{15}$$

where C_0 is the total initial AMD of the system and $\Lambda_{k,0} = m_k\sqrt{\mathcal{G}m_S a_{k,0}}$ is the initial circular angular momentum of planet k. To obtain expression (15), we assumed that planets b and c see no variation of their semimajor axis due to tidal migration and that e_c and e_b were equal, which is reasonable in first approximation due to the resonance. By inserting equations (14) and (15) into equation (12), we obtain a differential equation for a_d that gives results comparable to a secular complete integration (Pu & Lai 2019).

We draw 1000 initial conditions from the posterior distribution of Petigura et al. (2020). We plot in Fig. 5 the evolution of the period of planet d over 10 Gyr. The individual evolutions are in red, while the thick blue line corresponds to the averaged value.

The final orbital periods extend from 0 d (where planet d would be consumed by the star) to almost 2 d. It should be noted that for periods smaller than 0.4 d (semimajor axis of about 0.01 au), the decay is expected to be faster due to stellar tides that are neglected in this analysis. The typical outcome is the formation of an ultrashort-period planet with an orbit of about a day. The final orbit of planet d is mainly determined by the mass of planet d and the initial AMD. For larger AMD or smaller mass m_d, the final orbit is shorter.

We plot in Fig. 6, the resulting distribution of planet b eccentricity[5] and of planet d period at $t = 0$, 500 Myr and at $t =$ 2 Gyr. We see that even after a few hundreds of Myr, the decay of the eccentricity and orbital period are general and significant. After 2 Gyr, the eccentricity of planet b is smaller than 0.1 in 85 per cent of the simulations. In the simulations where planet d does not migrate up to the star, the orbital decay is stopped because the AMD reservoir has been emptied, that is the outer planets' orbits have been circularized.

[4]This is true as long as the planet spins are negligible with respect to the orbital angular momentum

[5]We recall that planet c is assumed to have the same eccentricity as planet b at all times.

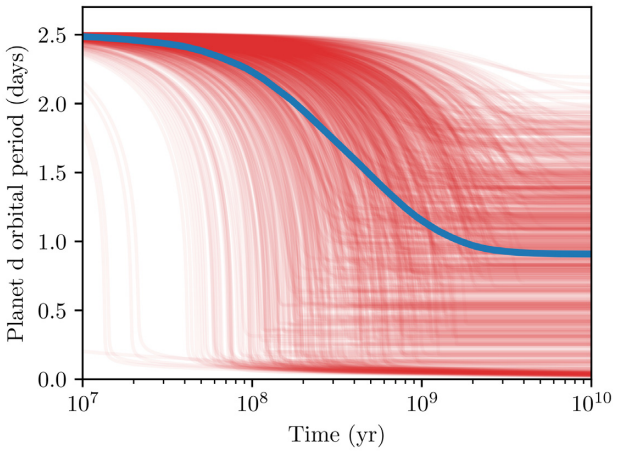

Figure 5. Planet d period evolution due to low-eccentricity tidal migration for 1000 initial conditions drawn from the three planet best fit. The blue curve is the average value. The spread is explained by the range of tidal lag times explored, the uncertainties on planet d's mass and the system's initial total AMD.

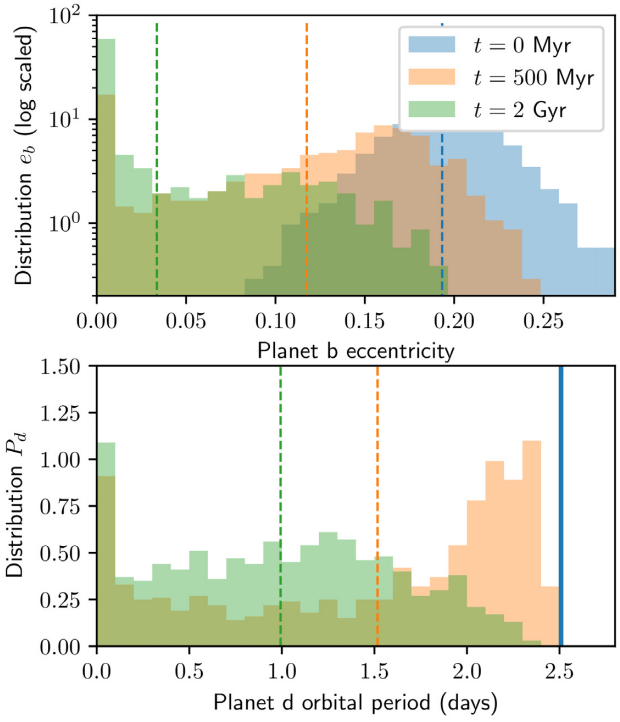

Figure 6. Distribution of planet b eccentricity (top panel) and planet d orbital period (bottom panel) at various times. In the second panel, the initial period is represented by a blue thick line. The dashed vertical lines correspond to the mean values at the given time. Note the log scale in the first panel.

More importantly, the final state is reached within a few hundred Myr. We define the half-decay time T_{hf} as the time such that planet d has undergone half of its orbital decay over 10 Gyr. The median half-decay time is $T_{\mathrm{hf}} = 472$Myr and 80 per cent of the initial conditions have $T_{\mathrm{hf}} < 1$Gyr.

3.2 Tidal decay in the past history of the system

We also considered the case where planet d started on a wider orbit and is currently experiencing tidal decay. We run the same model but with planet d starting with a period of 3.5 d, correcting the total AMD such that the system keeps the same total angular momentum. This initial period is the largest one before planet d's orbit crosses planet b's. After 2 Gyr, only 30 per cent of the systems have planet d with a period larger than 2.4 d and $e_b > 0.1$. The systems compatible with today's observations give a constrain on planet d tidal lag. The 1σ upper limit is $\Delta t_{L,d}^{86\text{ per cent}} = 130$ s (which corresponds to a quality factor of 180 at the current orbit). The constraints become stronger if the system is older than 2 Gyr.

It results that it may be possible that the observed system is on its way to circularize in the next billion of years. Such a scenario necessitates a very particular initial configuration where planet d is originally on an orbit at the limit of instability.

4 TRULY ECCENTRIC? TENSIONS BETWEEN THE OBSERVATIONS AND THE THEORY

The observations for this system are very precise and from multiple sources. The planets were detected thanks to the photometry from the K2 campaign (Armstrong et al. 2015; Sinukoff et al. 2016). The orbital elements and masses are also constrained by RV data and TTV obtained 2 yr after the *K2* campaign. Petigura et al. (2020) perform a photodynamical fit that forward model the light curve. Given the posterior distribution obtained, a close to circular, three planet model is strongly ruled out. Besides, the eccentricity cannot be attributed to a bias in the fitting model. Indeed, the eccentricities and periapsis argument are parametrized as $\{\sqrt{e}\cos\omega, \sqrt{e}\sin\omega\}$ such that the prior is uniform in eccentricity (Eastman, Gaudi & Agol 2013). The eccentricity priors as well as the photodynamical modelling have been used in a number of previous studies. In particular, if close to circular solutions provided a fit as good as the eccentric ones, the photodynamical model would have selected them.

In the limit of low eccentricities, the TTV signal is mainly affected by the distance to the nominal resonance $\delta = \frac{2P_c}{3P_b} - 1$ and the variable Y_1 (Lithwick, Xie & Wu 2012; Hadden & Lithwick 2016), but almost not by Y_2. This is the reason why the constraint on Y_1 is much better than the one on Y_2. Note that the formalism from Lithwick et al. (2012) is developed for close but out of resonance planets. While Y_1 has a much greater effect on the TTVs than Y_2, the photodynamical model can extract more information from the TTV signal for moderate eccentricities. Indeed, we can show that the value of Y_2 as a strong influence on the obtained TTVs. We draw 20 systems from the Monte Carlo Markov Chain (MCMC) posterior and compute their transit times in numerical simulations. We then refit the observed transits while forcing Y_2 to remain small ($\lesssim 0.03$) through numerical simulations and keep the best fit obtained. In practice, we perform a non- linear least-squares fit on the transit times using a cost function defined as $\chi^2 = \frac{1}{2}\sum_j \left(T_j^{\rm mod} - T_j^{\rm obs}\right)^2/\sigma_j^2$. We force Y_2 to remain small by performing a first fit after adding a term in the cost function proportional to $|Y_2|^2$. We then take the result of this first fit as an initial condition to a second fit without penalization.

We checked that the close to circular systems were also inside the 3:2 MMR. Note that this experiment's purpose is only to highlight the influence of Y_2 on the TTVs. In particular, we do not take into account the information from the full photometry from *K2*. We take into account the RV constraints on the planet masses (section 4.1, Petigura et al. 2020).[6]

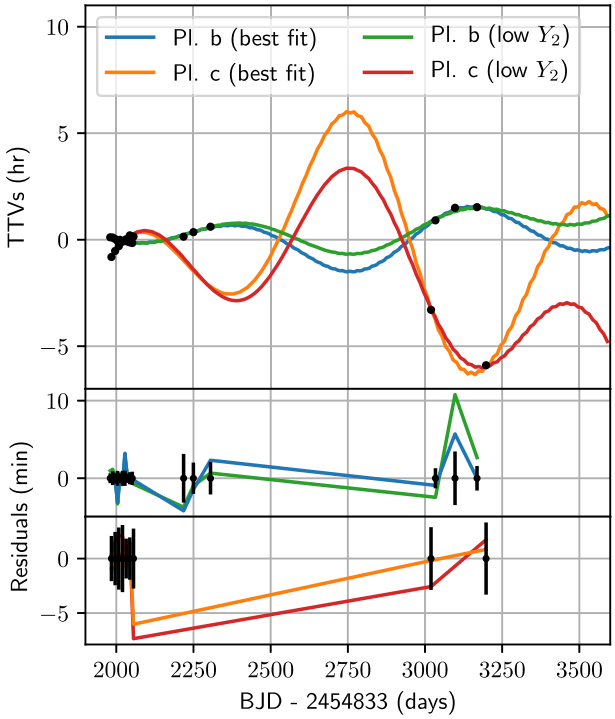

Figure 7. Synthetic TTV fits to the transit times. The 'best-fitting' curves (blue for planet b and orange for planet c) correspond to the best fit where the eccentricities are not constrained. These systems have moderate eccentricities. The low Y_2 TTVs (green for planet b and red for planet c), result from a fit to the transit times, while constraining the value of Y_2 (see the text). The pair b–c remains inside the MMR but the orbits are very close to circular. The observed transit times are plotted as black dots. In the bottom panels, we give the residuals to the observed transit times (in min).

For the eccentric system and its close to circular counterpart, we plot in the first panel of Fig. 7, the synthetic transit times as well as the observed times from the *K2* campaign[7] and from table 1 of Petigura et al. (2020). On the two last panels, we plot the residuals to the observed times. As expected, we see that the synthetic TTVs for the eccentric systems are consistent with the results obtained by Petigura et al. (2020). We note that the solutions where Y_2 was forced to remain small fit the transit times. However, we see that the two sets of curves behave qualitatively differently. We can also observe that the residuals are significantly larger for the close to circular fits with respect to the errors on the transit times. In particular, the eccentric fit is compatible with the final set of *Spitzer* data for planet b, whereas the transit times for the circular fit are at least 2σ away from the observations. It shows that such follow-up measurements, taken long after the initial planet discoveries are critical to the characterization of the system. Quantitatively, the goodness of fit of the eccentric, unconstrained fit is $\chi^2 = 17.7$ whereas it is $\chi^2 = 27.3$ for the close to circular ones.

[6]Fitting the transits without constraining the masses leads to systems where planet c mass is of order 20 $M_\oplus$, whereas the RVs give an upper mass of 10.2 $M_\oplus$ (at 95 per cent confidence). The fit without the constraints were not leading to a significant cost improvement.

[7]The *K2* times and the associated errors were estimated in Narita et al. (2015).

This small experiment confirms the results from the photo-dynamical modelling: the current observations favour eccentric orbits over close to circular ones. It should also be noted that the photodynamical modelling of the *K2* light curve done in Petigura et al. (2020) also incorporates information on the transit durations that is independent on the Y_1 measurement (Kipping 2010). While Petigura et al. (2020) ruled out $Y_2 = 0$ at 4σ formal significance, we acknowledge the possibility of errors due to model-misspecification. The fact that Y_2 factors so critically into the system's dynamical interpretation motivates additional observations by the exoplanet community.

Petigura et al. (2020) already noticed that the architecture of the system was puzzling despite it being stable in numerical simulations. However, it appears from the previous section that the tidal dissipation make the current system's architecture harder to explain. Besides, the formation of the system remains unexplained. So one needs to explain how to fit the observations while ensuring that the system configuration can be observed after a few Gyr.

4.1 The formation challenge

We showed in Section 2.1 that K2-19 b and c are trapped in the 3:2 MMR with a small libration amplitude. Capture into MMR generally emerges from dissipative effects leading to convergent migration (Batygin 2015). The most common mechanism is migration within the protoplanetary disc (e.g. Cresswell & Nelson 2008; Pichierri, Batygin & Morbidelli 2019). Capture can also occurs due to convergent tidal migration (Papaloizou, Szuszkiewicz & Terquem 2018). However, both disc and tidal migration show shorter time-scales for eccentricity damping than for change in orbital period. Systems are thus capture close to circular orbits, an increase of the eccentricity while the system is in the resonance typically leads to an anti-aligned configuration as pointed out by Petigura et al. (2020).

In order to explain the present configuration, one has to imagine a mechanism where the planet's eccentricity vectors are not damped to zero but to a common value. In this case, the capture can occur in the aligned configuration since the resonant dynamics and the capture mainly depend on Y_1 (equation 22 and fig. 7, Batygin 2015). Migration in eccentric disc has been studied theoretically (Papaloizou 2002), but eccentric discs arise only in the presence of large planets (Teyssandier & Ogilvie 2016) or for circumbinary discs. Moreover, eccentricities close to 0.2 leads to an outward migration (D'Angelo, Lubow & Bate 2006), which seems at odds with the short period of planets b and c. In any way, it is clear that the formation of the three planets around K2-19 remains a challenge that does not fit the classical scenarios.

4.2 New constraints from tidal dissipation

We have shown in Section 3 that taking into account tides is critical to understand the long-term evolution of this system. Indeed, the best-fitting orbital solution is stable in the presence of purely gravitational interactions over long time-scales. However, the secular coupling between planet d and the resonant pair (see Section 2.3) leads to a strong tidal dissipation in the inner planet. Over a few hundreds Myr, the outer planets' AMD is depleted and planet d experiences a period decay. If the system had truly formed as we see it today, we would expect to observe the outer planets on circular orbits and the inner one on a shorter orbit.

Yet, the current system configuration might be explained in presence of tidal decay. However, it implies that planet d orbital period was originally larger (up to 3.5 d) and that the three planets started on eccentric orbits with planets d and b at the limit of the orbit crossing. It also requires that the tidal lag time of planet d is smaller than 130 s (or that the quality factor is larger than 180), a value that is not incompatible with our understanding of tides in rocky bodies but that still gives a constraint on the dissipation rate. Lower quality factors are strongly ruled out. Such a fine tuning of the original configuration is necessary to explain the observed architecture if the system only hosts three planets.

In this work, we have not taken into account the dissipation in planets b and c because of the poor constraints on tidal dissipation in gaseous planets. However, works on on tidal dissipation for systems in MMR (e.g. Delisle et al. 2012, 2014) have shown that the resonance is often broken before the planets circularization. Such studies could give an additional constraint on the system.

4.3 A fourth planet?

When it is hard to reconcile the observations to the theory, it is common to explore the possibility that the planets motion can be perturbed by an unseen companion. From Le Verrier's work on Neptune to the recent Planet 9 hypothesis (Batygin et al. 2019), this approach is historically tied to the progresses in our understanding of the Solar system because of the very precise constraints on the planets' motion. However, the method have been applied with success also in the context of exoplanet dynamics. One can cite the example of Kepler-56 where the 40 deg obliquity of the two transiting planets is due to a distant planetary companion (Huber et al. 2013; Otor et al. 2016). But the most obvious application to exoplanets is the TTV method itself that allows us to find non-transiting planets, most of the time in resonance with a transiting one (Kepler-88, the 'King of TTVs' is an example of a system where a non-transiting planet perturbing the motion of Kepler-88b, Nesvorný et al. 2013).

The photodynamical fit strongly reject solutions with three planet on circular orbits. Nevertheless, it remains possible that the model is misspecified, which would be the case if, for instance, the TTVs are affected by a fourth planet in the system. In this case, the orbits of the observed planets b, c, and d might be close to circular at the expense of the addition of another planet in the resonant chain. Indeed, a few Earth masses planet trapped in an inner resonance with planet b can have significant TTVs contribution, while being non-transiting or even not being detected due to its small radius. We also point out that the TTV coverage of Petigura et al. (2020) is sparse, especially compared to TTV data sets from the prime *Kepler* mission. This data set had timing measurements over three distinct epochs (the *K2* campaign and two sets from *Spitzer*). We expect sparse data sets to be more susceptible to model misspecification errors and encourage additional transit time measurements.

While it will necessitate more transit observations in the future to verify such a claim, it should be noted that it is possible to add a planet between planets d and b without destabilizing the system. Indeed, we show the positions of the planets alongside the resonances 2:1 and 3:2 with planet b in Fig. 8. Another planet in 3:2 or 2:1 resonance with planet b is consistent with the 'peas in a pod' pattern observed in the architecture of the *Kepler* systems (Weiss et al. 2018). Moreover, assuming this unseen planet is in a 2:1 resonance with planet b leads to a period ratio of 1.58 with planet d, which is just wide of the 3:2 resonance. In other words, the whole system could have been placed into a four planet resonant chain during its formation before tidal effects broke the resonance

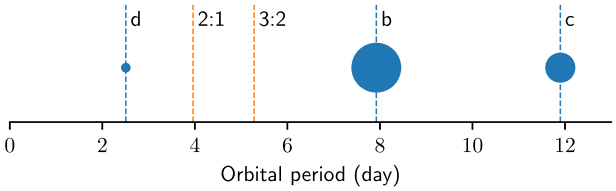

Figure 8. Architecture of the system K2-19 including the inner 2:1 and 3:2 MMR with planet b. The size of the planets is proportional to their radius.

with the innermost planet as it has been proposed by Millholland & Laughlin (2019) or Pichierri et al. (2019).

5 CONCLUSIONS AND DISCUSSIONS

In systems such as K2-19, the precise orbital parameters obtained by TTVs allow for rich dynamical studies that can provide a lot of insight on to the system history and configuration. Such systems act as laboratories to test theories of formation and dynamical evolution.

Following their observations, Petigura et al. (2020) conclude that K2-19's two outer planets are very close to the 3:2 MMR but due to their large aligned eccentricity, the classical resonant angles are not librating. A system with such a configuration is a challenge for classical planet formation scenarios. Indeed, planets close to MMR tend to be captured due to type I migration during the disc lifetime (Cresswell & Nelson 2008). Besides, migration is very effective to damp planet's eccentricities.

We have shown in Section 2.1 that by considering the true resonant variables of the system that is a combination of the two complex eccentricities, the system rapid dynamics are well explained by the integrable first-order model. Besides, the very small libration amplitude of the resonant variable (fig. 2) strengthens the classical scenario of a smooth capture through disc migration (Batygin 2015). We also see that the resonant variable is more constrained than the two eccentricities as it is expected for systems presenting TTVs (Hadden & Lithwick 2016). In particular, we want to highlight that in the context of orbital fit with such large eccentricities, the classical methods to spot an MMR such as monitoring the classical resonant angles (equation 1) is not reliable. A resonant configuration can also exist even if the two orbits are not anti-aligned.

We then studied the entire system rather than only the two outer more massive planets. The fitted configuration leads to a very strong secular coupling between the inner terrestrial planet d and the pair b and c. The coupling does not disrupt the MMR but leads to eccentricities of the order of 0.35 for the inner planet. In particular, this planetary system's architecture is long-lived in the presence of purely *N*-body interactions.

Because planet d orbits in about 2.5 d around its host star, it is subject to large tidal effects. The tides raised on planet d tend to circularize its orbit at the expense of a period decay. Following the low-eccentricity migration model presented in Pu & Lai (2019), we show that the two outer planets transfer their AMD to the inner planet through the secular coupling. As a result, the inner planet continues to decay up until the point where tidal and general relativity precession decouple it from the outer planets or if the outer planets run out of AMD. The typical time-scale of the process is less than 500 Myr, whereas the system is expected to be billions of years old. The system's current architecture remains compatible with the tidal decay if planet d started in a longer orbit, at the limit of orbit crossing with planet b. Note that in the absence of planet d, it would be much harder to rule out the aligned eccentric resonant configuration due to the poor constraint we have on the dissipation on to gaseous planets.

Even though the photodynamical fit gives a configuration that can only be maintained for a short amount of time with respect to the system lifetime, the observations have to be explained. While biases in eccentricity determination are known and have been quantified in RV observations (Anglada-Escudé, López-Morales & Chambers 2010; Hara et al. 2019), no such study has been carried for TTVs systems. One could speculate on the fact that another undiscovered planet in the system can affect the outer planets periods. Indeed, in the picture of the 'peas in a pod' systems (Weiss et al. 2018), the system is compatible with the presence of another planet between planets d and b. If such a non-transiting planet could also be in resonance with planets b and c and lead to TTV unaccounted for. However, the presence of an eventual fourth planet would need to be confirmed by more measurements of planets b and c transits.

The detailed analysis of the K2-19 system has revealed even richer dynamics than originally reported. Taking into account the dissipative effects also appears to be crucial for the understanding of the system history. Nevertheless, the system formation remains mostly unexplained. Future photometric or RV monitoring will be crucial to unveil the nature of this system.

ACKNOWLEDGEMENTS

The authors wish to thank the anonymous referee, Konstantin Batygin, Trevor David, Alexander Mustill, and Gabriele Pichierri for helpful comments and discussions. MD and AP are supported by the project grant 2014.0017 'IMPACT' from the Knut and Alice Wallenberg Foundation. AJ and AP were supported by the European Research Council under ERC Consolidator grant agreement 724687-PLANETESYS, the Swedish Research Council (grant 2018-04867), and the Knut and Alice Wallenberg Foundation (grants 2014.0017 and 2017.0287).

DATA AVAILABILITY

The data and code used to generate the plots in this article will be shared on reasonable request to the corresponding author.

REFERENCES

Agol E., Steffen J., Sari R., Clarkson W., 2005, MNRAS, 359, 567
Alexander M. E., 1973, Ap&SS, 23, 459
Anglada-Escudé G., López-Morales M., Chambers J. E., 2010, ApJ, 709, 168
Armstrong D. J. et al., 2015, A&A, 582, A33
Batygin K., 2015, MNRAS, 451, 2589
Batygin K., Morbidelli A., 2013, A&A, 556, A28
Batygin K., Adams F. C., Brown M. E., Becker J. C., 2019, Phys. Rep., 805, 1
Bitsch B., Izidoro A., Johansen A., Raymond S. N., Morbidelli A., Lambrechts M., Jacobson S. A., 2019, A&A, 623, A88
Blanes S., Casas F., Farrés A., Laskar J., Makazaga J., Murua A., 2013, Appl. Numer. Math., 68, 58
Correia A. C. M., Boué G., Laskar J., Rodríguez A., 2014, A&A, 571, A50
Cresswell P., Nelson R. P., 2008, A&A, 482, 677
D'Angelo G., Lubow S. H., Bate M. R., 2006, ApJ, 652, 1698
Darwin G. H., 1880, RSPT, 171, 713
Deck K. M., Payne M., Holman M. J., 2013, ApJ, 774, 129

Delisle J.-B., Laskar J., Correia A. C. M., Boué G., 2012, A&A, 546, A71
Delisle J.-B., Laskar J., Correia A. C. M., 2014, A&A, 566, A137
Eastman J., Gaudi B. S., Agol E., 2013, PASP, 125, 83
Efroimsky M., Makarov V. V., 2014, ApJ, 795, 6
Fabrycky D. C. et al., 2014, ApJ, 790, 146
Ferraz-Mello S., 2007, Astrophysics and Space Science Library, Vol. 345, Canonical Perturbation Theories. Springer, New York, NY
Goldreich P., Soter S., 1966, Icarus, 5, 375
Hadden S., 2019, AJ, 158, 238
Hadden S., Lithwick Y., 2016, ApJ, 828, 44
Hara N. C., Boué G., Laskar J., Delisle J.-B., Unger N., 2019, MNRAS, 489, 738
Henrard J., Lemaitre A., 1983, Celest. Mech., 30, 197
Henrard J., Lemaitre A., Milani A., Murray C. D., 1986, Celest. Mech., 38, 335
Holman M. J., Murray N. W., 2005, Science, 307, 1288
Howell S. B. et al., 2014, PASP, 126, 398
Huber D. et al., 2013, Science, 342, 331
Hut P., 1981, A&A, 99, 126
Izidoro A., Ogihara M., Raymond S. N., Morbidelli A., Pierens A., Bitsch B., Cossou C., Hersant F., 2017, MNRAS, 470, 1750
Izidoro A., Bitsch B., Raymond S. N., Johansen A., Morbidelli A., Lambrechts M., Jacobson S. A., 2019, preprint (astro-ph/1902.08772)
Kipping D. M., 2010, MNRAS, 407, 301
Lambrechts M., Morbidelli A., Jacobson S. A., Johansen A., Bitsch B., Izidoro A., Raymond S. N., 2019, A&A, 627, A83
Laskar J., 1990, in Les Méthodes Modernes de La Mécanique Céleste. Modern Methods in Celestial Mechanics. p. 89, San Francisco Book Company, Paris, France
Laskar J., 1997, A&A, 317, L75
Laskar J., Petit A. C., 2017, A&A, 605, A72
Laskar J., Boué G., Correia A. C. M., 2012, A&A, 538, A105
Lithwick Y., Xie J., Wu Y., 2012, ApJ, 761, 122
Makarov V. V., Efroimsky M., 2014, ApJ, 795, 7
Mardling R. A., 2007, MNRAS, 382, 1768
Mayor M., Queloz D., 1995, Nature, 378, 355
Millholland S., Laughlin G., 2019, Nat. Astron., 3, 424
Morbidelli A., 2002, Modern Celestial Mechanics: Aspects of Solar System Dynamics. Taylor & Francis, Milton Park, UK
Mustill A. J., Wyatt M. C., 2011, MNRAS, 413, 554
Narita N. et al., 2015, ApJ, 815, 47
Nesvorný D., Kipping D., Terrell D., Hartman J., Bakos G. Á., Buchhave L. A., 2013, ApJ, 777, 3
Ogilvie G. I., 2014, ARA&A, 52, 171
Otor O. J. et al., 2016, AJ, 152, 165
Papaloizou J. C. B., 2002, A&A, 388, 615
Papaloizou J. C. B., Szuszkiewicz E., Terquem C., 2018, MNRAS, 476, 5032
Petigura E. A. et al., 2020, AJ, 159, 2
Petit A. C., Laskar J., Boué G., 2017, A&A, 607, A35
Pichierri G., Batygin K., Morbidelli A., 2019, A&A, 625, A7
Pu B., Lai D., 2019, MNRAS, 488, 3568
Rein H., Liu S.-F., 2012, A&A, 537, A128
Rein H., Tamayo D., Brown G., 2019, MNRAS, 489, 4632
Sessin W., Ferraz-Mello S., 1984, Celest. Mech., 32, 307
Sinukoff E. et al., 2016, ApJ, 827, 78
Teyssandier J., Ogilvie G. I., 2016, MNRAS, 458, 3221
Weiss L. M. et al., 2018, AJ, 155, 48
Winn J. N., Fabrycky D. C., 2015, ARA&A, 53, 409

APPENDIX A: MEAN MOTION RESONANCE DYNAMICS

In this section, we briefly derive the first-order integrable model for the $p+1$:p MMR. The reader interested in a recent detailed analysis should refer to Batygin & Morbidelli (2013), Deck et al. (2013), Petit et al. (2017), and Hadden (2019). The model was initially developed by Henrard & Lemaitre (1983), Sessin & Ferraz-Mello (1984), and Henrard et al. (1986). We consider two planets of mass m_1 and m_2 orbiting a star of mass m_0 in a plane (the spatial case is treated similarly). The Hamiltonian in democratic heliocentric coordinates is (e.g. Morbidelli 2002)

$$\mathcal{H} = \sum_{k=1}^{2} \frac{||\tilde{\boldsymbol{r}}_k||^2}{2m_k} - \frac{\mu m_k}{r_k} + \frac{||\tilde{\boldsymbol{r}}_1 + \tilde{\boldsymbol{r}}_2||^2}{2m_0} - \frac{\mathcal{G} m_1 m_2}{r_{12}}, \tag{A1}$$

where $\tilde{\boldsymbol{r}}_k = m_k \dot{\boldsymbol{r}}_k$ is the barycentric momentum, $\boldsymbol{r}_k$ the heliocentric position $\mathcal{G}$ is the gravitational constant, and $\mu = \mathcal{G} m_0$. We may express $\mathcal{H}$ in terms of the complex Poincaré coordinates (e.g. Laskar 1990)

$$\begin{aligned}
\Lambda_k &= m_k \sqrt{\mu a_k}, & \lambda_k;\\
C_k &= \Lambda_k \left(1 - \sqrt{1 - e_k^2}\right), & -\varpi_k;\\
\sqrt{C_k} e^{-\imath \varpi_k}, & & \imath \sqrt{C_k} e^{\imath \varpi_k};
\end{aligned}$$

where a_k is the semimajor axis, e_k the eccentricity, λ_k the mean longitude and ϖ_k the longitude of periapsis of planet k. Note that the last two lines are redundant and both set of variables can be used to obtain the Hamiltonian equations. Expressed in these variables, the Hamiltonian takes the form $\mathcal{H}_0 + \varepsilon \mathcal{H}_1$, where $\mathcal{H}_0$ is the Keplerian part

$$\mathcal{H}_0 = -\frac{\mu^2 m_1^3}{2\Lambda_1^2} - \frac{\mu^2 m_2^3}{2\Lambda_2^2} \tag{A3}$$

and $\varepsilon \mathcal{H}_1$ is the perturbation part and depends on all the coordinates. The small parameter $\varepsilon = (m_1 + m_2)/m_0$ is introduced explicitly to emphasize the scale difference.

In order to obtain an integrable model for the $p+1$:p MMR, we carry out a canonical transformation such that the new coordinates are (e.g. Petit et al. 2017)

$$\begin{aligned}
\Gamma &= \tfrac{p+1}{p}\Lambda_1 + \Lambda_2, & \theta_\Gamma &= p(\lambda_1 - \lambda_2), ;\\
G &= \Lambda_1 + \Lambda_2 - C_1 - C_2, & \theta_{\rm res} &= (p+1)\lambda_2 - p\lambda_1;\\
x_k &= \sqrt{C_k} e^{\imath(\varpi_k - \theta_{\rm res})}, & \imath \bar{x}_k &= \imath \sqrt{C_k} e^{-\imath(\varpi_k - \theta_{\rm res})};
\end{aligned}$$

Γ has been called in the literature the scaling factor (Sessin & Ferraz-Mello 1984), G is the total angular momentum. Because of the d'Alembert relations, the Hamiltonian does not depend explicitly on $\theta_{\rm res}$ (i.e. the angular momentum is conserved). The two resonant angles are $\varpi_k - \theta_{\rm res}$ (see equation 1). We then expand the perturbation $\varepsilon \mathcal{H}_1$ in power series of x_k and Fourier series of θ_Γ and only keep the first-order terms. The next step consists in averaging the motion over the fast angle θ_Γ. This operation is also a canonical transformations and the new coordinates are ε close to the old ones. They correspond to the average coordinates over a Keplerian orbit. The resulting Hamiltonian no longer depends on θ_Γ. As a result, Γ is a constant of the averaged system. Note that the inverse transformation of equation (A4) allow to express Λ_k as a function of the total AMD, C and the constants of motion Γ and G.

The perturbation $\varepsilon \mathcal{H}_1$ then takes the form

$$\varepsilon \mathcal{H}_1 = \varepsilon R_1(x_1 + \bar{x}_1) + \varepsilon R_2(x_2 + \bar{x}_2), \tag{A5}$$

where

$$R_1 = -\frac{\gamma}{1+\gamma} \frac{\mu^2 m_2^3}{\Lambda_2^2} \frac{1}{2} \sqrt{\frac{2}{\Lambda_1}} \mathcal{R}_1(\alpha) \tag{A6}$$

and

$$R_2 = -\frac{\gamma}{1+\gamma}\frac{\mu^2 m_2^3}{\Lambda_2^2}\frac{1}{2}\sqrt{\frac{2}{\Lambda_2}}\mathcal{R}_2(\alpha) \tag{A7}$$

with $\gamma = m_1/m_2$ and $\alpha = a_1/a_2$,

$$\mathcal{R}_1(\alpha) = -\frac{\alpha}{4}\left(3b^p_{3/2}(\alpha) - 2\alpha b^{p+1}_{3/2}(\alpha) - b^{p+2}_{3/2}(\alpha)\right), \tag{A8}$$

$$\mathcal{R}_2(\alpha) = \frac{\alpha}{4}\left(3b^{p-1}_{3/2}(\alpha) - 2\alpha b^{p}_{3/2}(\alpha) - b^{p+1}_{3/2}(\alpha)\right) + \frac{1}{2}b^p_{1/2}(\alpha). \tag{A9}$$

The opposite signs of $\mathcal{R}_1$ and $\mathcal{R}_2$ should be noted. In the two previous expressions, $b^k_s(\alpha)$ are the Laplace coefficients that can be expressed as

$$b^k_s(\alpha) = \frac{1}{\pi}\int_{-\pi}^{\pi}\frac{\cos(k\phi)}{\left(1-2\alpha\cos\phi+\alpha^2\right)^s}\mathrm{d}\phi \tag{A10}$$

for $k > 0$. For $k = 0$, a 1/2 factor has to be added in the second-hand member of equation (A10). Note that for $p = 1$, that is the 2:1 MMR, a contribution from the indirect part (due to the reflex motion of the star) should be added (Delisle et al. 2012). Because we restrict the expansion to the first order, all the coefficients are constant and evaluated at the Keplerian resonance, $\alpha = \alpha_0 = (p/(p+1))^{2/3}$.

The integrable Hamiltonian is then obtained by a final transformation proposed by Sessin & Ferraz-Mello (1984) and Henrard et al. (1986) and generalized by Hadden (2019) to resonances of arbitrary order. Geometrically, it consists in a rotation of the coordinates x_1 and x_2. We define

$$\begin{aligned} y_1 &= \frac{R_1}{\sqrt{R_1^2+R_2^2}}x_1 + \frac{R_2}{\sqrt{R_1^2+R_2^2}}x_2 \\ y_2 &= \frac{R_2}{\sqrt{R_1^2+R_2^2}}x_1 - \frac{R_1}{\sqrt{R_1^2+R_2^2}}x_2. \end{aligned} \tag{A11}$$

Let us define $I_k = y_k\bar{y}_k$. I_2 now becomes a constant of motion and $C = I_1 + I_2$. I_1 and I_2 do not depend on the resonant angles but only on $\Delta\varpi$. Indeed one has

$$\begin{aligned} I_1 &= \tfrac{1}{R_1^2+R_2^2}\left(R_1^2C_1 + R_2^2C_2 + 2R_1R_2\sqrt{C_1C_2}\cos(\Delta\varpi)\right), \\ I_2 &= \tfrac{1}{R_1^2+R_2^2}\left(R_2^2C_1 + R_1^2C_2 - 2R_1R_2\sqrt{C_1C_2}\cos(\Delta\varpi)\right). \end{aligned} \tag{A12}$$

Finally, we expand the Keplerian part close to the circular Keplerian resonance given the scaling factor Γ and the angular momentum G

$$\mathcal{H}_0 = \frac{\mathcal{K}_2}{2}(C-\Delta G)^2, \tag{A13}$$

where

$$\frac{\mathcal{K}_2}{2} = -\frac{3n_2}{2\Lambda_2}(p+1)^2\frac{\gamma+\alpha}{\alpha}, \tag{A14}$$

$n_2 = 2\pi/P_2$ being the mean motion and

$$\Delta G = \frac{\Gamma}{p+1}\frac{p\gamma+(p+1)\alpha_0}{\gamma+\alpha_0} - G. \tag{A15}$$

The integrable Hamiltonian plotted in Fig. 2 has the form

$$\mathcal{H} = \frac{\mathcal{K}_2}{2}(I_1+I_2-\Delta G)^2 + 2\varepsilon\sqrt{R_1^2+R_2^2}\sqrt{I_1}\cos(\theta_1) \tag{A16}$$

where θ_1 is the argument of y_1. Such a Hamiltonian is called the second fundamental model of resonance. We refer to the previously cited papers and to Ferraz-Mello (2007) for a complete description of the dynamics.

When plotting the Hamiltonian level curves in Fig. 2, we choose the value of the parameters from the short-term integration shown in grey. This choice is motivated by the fact that the posterior values of I_1 and $I_2 - \Delta G$ are correlated. Indeed, while the uncertainties on I_1 are much smaller than the uncertainties on I_2, it turns out, that the uncertainties on the quantity $I_1 + I_2 - \Delta G$ are even smaller. The ratio of the standard deviations of $I_1 + I_2 - \Delta G$ and I_1 is 0.07. Since the shape of the resonance is affected by small variations of $I_2 - \Delta G$, the values associated to the integration are more faithful to the actual dynamics. We also emphasize that it is critical to compute I_2 with the exact expression and not the linear approximations for $\tilde{e}_k$ as the approximation leads to a significant deformation of the phase space.

As claimed in Section 2.1, $\theta_2 = \arg(Y_2)$ precesses at the same frequency as $\theta_{\rm res}$. Indeed, by definition of the canonical variables, we have

$$\dot{\theta}_2 = \frac{\partial\mathcal{H}}{\partial I_2} = \mathcal{K}_2(C-\Delta G) = \frac{\partial\mathcal{H}}{\partial G} = \dot{\theta}_{\rm res}. \tag{A17}$$

The frequency can be related to the distance to the Keplerian resonance $\delta = pn_1/((p+1)n_2) - 1$ and we have $\dot{\theta}_2 = -n_2\delta(p+1)$.

This paper has been typeset from a TEX/LATEX file prepared by the author.